Article

Review of Reduced-Order Models for Homogeneous CO_2 Nucleation in Supersonic and Hypersonic Expansion Flows

Philip A. Lax [1,*] and **Sergey B. Leonov** [1]

1   Aerospace and Mechanical Engineering, University of Notre Dame, Notre Dame, IN 46556, USA; sleonov@nd.edu
*   Correspondence: plax@nd.edu

Abstract: Several classical and non-classical reduced-order nucleation rate models are presented and compared to experimental values for the homogeneous nucleation rate of CO_2 in supersonic nozzles. The most accurate models are identified and are used in simulations of a condensing supersonic expansion flow. Experimental results for the condensation onset point of CO_2 in a variety of expansion facilities are presented and compared to simulations and to new data acquired at the SBR-50 facility at the University of Notre Dame.

Keywords: homogeneous nucleation; reduced order models; classical nucleation theory; carbon dioxide; supersonic flow; hypersonic flow

1. Introduction

The maximum Reynolds number achievable by ground test facilities is often limited by liquefaction of the working fluid at low static temperatures and/or high static pressures. For example, the minimum stagnation temperature of the AFOSR–Notre Dame Large Mach 6 Quiet Tunnel currently in development at the University of Notre Dame is $T_0 = 430$ K [1] in order to prevent the creation of a supersaturated gas state. However, condensation is a finite-rate process with extremely low nucleation rates near the binodal, at which point the bulk liquid and saturated vapor are in chemical equilibrium. Combined with the short residence times of supersonic and hypersonic facilities, homogeneous nucleation is not appreciable for static temperatures $\Delta T = 13$–22 K [2–4] below the binodal. Supercooling of just 13 K will result in a decrease in the minimum stagnation temperature of 120 K at Mach 6, and a corresponding increase in the maximum Reynolds number. This has significant implications for the study of hypersonic boundary layer laminar-turbulent transition, among other research interests.

Hypersonic ground test facilities commonly use dried and filtered air, which is an effective and economical working fluid. However, the concentration of carbon dioxide in dried air remains near atmospheric levels, which are currently 415 ppm and increasing at about 2.5 ppm per year [5]. This vapor condenses within the nozzle of hypersonic expansion facilities, providing condensation nuclei for the later heterogeneous conden-sation of oxygen and nitrogen. Heterogeneous nucleation occurs at a lower saturation ratio and a lower degree of supercooling at condensation onset as compared to homoge-neous nucleation. It has previously been shown [6] that a gaseous impurity at similar concentrations to atmospheric CO_2 is sufficient for the reduced supercooling observed in the studies of Refs. [7–9]. Accurate modeling of the carbon dioxide nucleation process is required as a prerequisite for reliable estimates for heterogeneous condensation, and thus the minimum achievable stagnation temperature and maximum Reynolds number in a hypersonic expansion facility.

While CO_2 nucleation has been studied extensively [10–15], the authors are not aware of any reduced-order model identified in available literature that can be readily applied with accuracy sufficient for flowfield simulations. While some nucleation models are

compared to experimental data in Ref. [10], no model considered yields accurate predictions for the nucleation rate.

Classical nucleation theory (CNT), the oldest and most simple nucleation theory, is often used in flowfield simulations [16,17] and even in some molecular dynamics simulations [18–20]. However, the assumptions of CNT are not valid for small molecular clusters formed in supersonic and hypersonic expansion flows. The predictions of CNT are only approximately accurate in a relatively narrow temperature range [21,22], with the theory overestimating the nucleation rate at higher temperatures and underestimating the nucleation rate by up to 25 orders of magnitude at lower temperatures common for condensable expansion flows [6]. The failure of CNT to accurately predict the nucleation rate of many fluids is fundamentally due to the fact that macroscopic approximations can not be applied to nucleating clusters composed of small numbers of discrete molecules without significant error [23]. While corrections to CNT such as Tolman theory [24] and an effective surface tension [25] yield more reasonable nucleation rate values, these corrections are temperature dependent, and since they are usually constants tuned to a specific experimental dataset they do not have wider applicability. While the nucleation rate and cluster free energy barrier may be estimated by appropriate molecular dynamics simulations [26,27], these simulations are highly detailed. Due to the large computational resources required, direct numerical simulations are usually only attempted at a few specific gas states with exceedingly high nucleation rates, usually about 10^{30} m^{-3}s^{-1} [19,28], which is about a factor of 10^7 greater than the average nucleation rate for most supersonic expansion flows [29].

Properties of small numbers of discrete molecules in van der Waals clusters are distinct from those of bulk fluids or solids [30–32]. For example, small solid-like clusters of CO_2 undergo a transition from an icosahedral structure to the bulk cubic structure at about $N = 25$ [33,34]. Cluster properties often lie between those of the gas and the bulk liquid or solid, making them a form of matter distinct from bulk gases, liquids, or solids. Clusters are sometimes referred to as a fifth state of matter [35]. It is well known that a liquid-like to solid-like phase transition, analogous to the bulk melting transition [36], occurs in molecular clusters at temperatures decreasing from the bulk value as the number of molecules in the cluster decreases. Approximate size-dependent phase diagrams have been produced for Lennard–Jones clusters [37,38]. A melt-like transition has been observed in molecular dynamics simulations for $(CO_2)_{13}$ at about T = 95 K [39] and for $(CO_2)_5$ at about T = 50 K [40]. Since critical CO_2 clusters considered here are composed of 5–6 molecules at temperatures greater than 50 K, nucleating clusters are considered to be liquid-like, and liquid state properties are used in the relevant nucleation models rather than solid state properties.

The objective of this work is a review and comparison of reduced order models available in the literature to the experimental results of CO_2 condensation onset.

2. Nucleation Theory

All gases undergo constant fluctuations at the microscale that result in the formation of molecular clusters [41,42], even subsaturated gases that may otherwise be considered ideal. The equilibrium number density of clusters composed of N molecules is

$$n_{N,e} = n_{\text{tot}} \exp\left(\frac{-\Delta F_N}{k_B T}\right), \tag{1}$$

where n_{tot} is the total number density of clusters of all sizes, and ΔF_N is the free energy barrier of cluster formation. Since clusters are usually rare compared to free molecules, n_{tot} is commonly approximated by n_v, the number density of vapor molecules obtained from an equation of state. It may be argued [43] that the cluster size distribution should be evaluated for the saturated equilibrium vapor regardless of the actual saturation ratio, in which case n_v may be replaced by $n_s = n_v/S$, where $S = n_v/n_s$ is the saturation ratio. For an ideal gas, $S = p_v/p_s$.

The free energy barrier is composed of two parts: a negative volume term corresponding to the creation of the new phase and a positive surface term corresponding to the creation of the phase boundary. The general behavior of ΔF in a supersaturated gas is to increase from zero to a positive maximum, and then decrease without bound towards negative infinity as $N \to \infty$. The cluster size for which $\partial \Delta F / \partial N = 0$ is referred to as the critical cluster, which is in unstable equilibrium with the surrounding vapor. The number of molecules in the critical cluster is thus defined by $(\partial \Delta F / \partial N)_{N=N_*} = 0$, where "$*$" refers to the critical cluster.

The principle of detailed balance for stationary cluster concentrations at constrained equilibrium requires that

$$\alpha_{N+1} n_{N+1,e} = \beta_N n_{N,e} \tag{2}$$

where α_N is the evaporation rate of molecules from the cluster and β_N is the impingement rate of molecules onto the cluster. The quasi-steady state nucleation rate is

$$J = \beta_N n_N - \alpha_{N+1} n_{N+1}, \tag{3}$$

which for a nonequilibrium supersaturated gas is positive. Combining Equations (2) and (3) and rearranging yields

$$\frac{J}{\beta_N n_{N,e}} = \frac{n_N}{n_{N,e}} - \frac{n_{N+1}}{n_{N+1,e}} \tag{4}$$

Summing from $N = 1$ to M results in the cancellation of all terms on the right hand side except for the first and last, yielding

$$J \sum_{N=1}^{M} \left(\frac{1}{\beta_N n_{N,e}} \right) = \frac{n_1}{n_{1,e}} - \frac{n_{M+1}}{n_{M+1,e}}. \tag{5}$$

The smallest cluster is formed with negligible time delay, so $n_1 \approx n_{1,e}$ or $n_1/n_{1,e} \approx 1$. Provided that M is large enough that negligibly few clusters of size M have yet to be formed, $n_{M+1} \ll n_{M+1,e}$ and $n_{M+1}/n_{M+1,e} \approx 0$, resulting in the form

$$J = \left[\sum_{N=1}^{M} \left(\frac{1}{\beta_N n_{N,e}} \right) \right]^{-1}. \tag{6}$$

The discrete summation may be approximated by an integral with doubly infinite bounds. Since $n_{N,e}$ has a sharp exponential minimum at the critical cluster, the free energy barrier may be approximated by a Taylor series expansion around N_*. Evaluating the integral results in the general form [43–45] for the steady state nucleation rate of a supersaturated gas,

$$J = n_v \beta_* Z \exp \left(\frac{-\Delta F_*}{k_B T} \right). \tag{7}$$

The molecular impingement rate onto a cluster may be approximated [43,46] by

$$\beta_N = n_v \left(\frac{3}{4\pi} \right)^{1/6} \left(\frac{6k_B T}{m_N} + \frac{6k_B T}{m_1} \right)^{1/2} \left(v_N^{1/3} + v_1^{1/3} \right)^2, \tag{8}$$

where m_N and m_1 are the mass and v_N and v_1 are the volume of the cluster and free molecule, respectively. The volume per molecule is approximated by the average volume per molecule in the liquid, $v_1 = m_1/\rho_l$, where ρ_l is the mass density of the saturated liquid. The Zel'dovich [47] factor,

$$Z = \left(\frac{-1}{2\pi k_B T} \frac{\partial^2 \Delta F}{\partial N^2} \right)^{1/2}, \tag{9}$$

is the integral result of the second order term of the Taylor series expansion of the free energy barrier, and may be approximated [48] by

$$Z = \left(\frac{\Delta F_*}{3\pi k_B T N_*^2} \right)^{1/2}. \tag{10}$$

Integral forms have been derived [49,50] for the transient nucleation rate. For the instantaneous expansion of a saturated gas into a supersaturated state, the transient nucleation rate [48] is

$$\frac{J_t}{J} = 1 - \exp\left(-\frac{t}{\tau_t} \right) \tag{11}$$

where the characteristic time is

$$\tau_t = \frac{1}{\beta_* Z^2}. \tag{12}$$

Since the characteristic time is typically on the order of 1–10 µs [44] for gases, the transient nucleation rate is approximated by the steady state nucleation rate.

2.1. Classical Nucleation Theory

The classical nucleation theory (CNT) expression for the free energy barrier of a cluster [43] is

$$\Delta F_N = s_1 N^{2/3} \sigma - N\Delta\mu \tag{13}$$

where $s_1 = (36\pi v_1^2)^{1/3}$ is the surface area per liquid molecule, $N^{2/3}$ is an approximation for the number of molecules at the surface of the cluster, σ is the surface tension, and $\Delta\mu$ is the difference in chemical potential between N molecules in the vapor and N molecules in the liquid cluster. CNT uses a capillarity approximation for the cluster in which the liquid is incompressible with uniform saturated liquid density n_l, the liquid makes a sharp interface with the vapor, and the surface tension is equal to that of the bulk liquid. For an ideal gas and incompressible fluid, the difference in chemical potential may be shown [43,51] to be

$$\Delta\mu = k_B T \ln(S) - v_1(p_v + p_c - p_s), \tag{14}$$

which includes a minor correction to account for the noncondensing carrier gas pressure p_c. The second term in this expression is much smaller than the first and is often omitted.

The surface tension σ of the cluster is usually approximated in CNT by the infinite plane surface tension of the saturated liquid σ_∞. However, surface tension is dependent on the curvature of the liquid surface [52–54]. The size dependence of surface tension may be estimated using Tolman's [52] equation,

$$\frac{\sigma}{\sigma_\infty} = \frac{1}{1 + 2\delta_T/r}, \tag{15}$$

where δ_T is the Tolman length and r is the radius of the spherical liquid droplet. It is assumed in the derivation of this expression that δ_T itself has no size dependence, which is strictly only true for clusters containing more than about 10^6 molecules [55]. However, it provides a useful first-order approximation for the surface tension of clusters. An estimate for the Tolman length obtained from the molecular theory of surface tension [56] is

$$\delta_T = \frac{2\pi\kappa_l\sigma_\infty}{5A}, \tag{16}$$

where κ_l is the isothermal compressibility of the liquid and A is a temperature dependent term defined in Equation (46). An estimate for the Tolman length obtained from molecular dynamics simulations [57] is

$$\frac{\delta_T}{r} = \left(\frac{0.7}{1 - T/T_c} - 0.9 \right) N^{-1/3}, \tag{17}$$

where T_c is the critical temperature of the fluid.

2.2. Self-Consistent Classical Nucleation Theory

It may be observed that when the CNT free energy barrier (Equation (13)) is used with the infinite plane surface tension to find the equilibrium number density of clusters (Equation (1)) that the free molecule number density is not recovered when $N = 1$ since $\Delta F_1 \neq 0$. This is corrected in self-consistent classical nucleation theory (SCCNT) [58,59] by modification of the CNT free energy barrier, resulting in

$$\Delta F_N = s_1\left(N^{2/3} - 1\right)\sigma - (N-1)\Delta\mu. \tag{18}$$

The change in the first term results from subtracting the surface energy of a single liquid molecule. The change in the second term results from using the saturated number density $n_s = n_v/S$ instead of n_v to find the number density of clusters and moving the Courtney [60] $1/S$ correction term into the exponential. The ratio of the SCCNT nucleation rate to the CNT nucleation rate is

$$\frac{J_{SCCNT}}{J_{CNT}} = \exp\left(\frac{s_1\sigma - \Delta\mu}{k_BT}\right), \tag{19}$$

which can be as low as 10^3 or as high as 10^{50} depending on the fluid and temperature, but in most cases is 10^{10-25} [58].

As noted by Reguera et al. [61], the value $N = 1$ corresponds to a hypothetical liquid cluster consisting of a single molecule, not a free vapor molecule. While physically a single molecule in isolation cannot be assigned a state, in CNT the pure vapor phase results when the liquid cluster vanishes, which corresponds to $N = 0$. Setting $N = 0$ in Equation (13) results in $\Delta F = 0$, and there is no inconsistency.

2.3. Mean-Field Kinetic Nucleation Theory

Kalikmanov's [44,62] mean-field kinetic nucleation theory (MKNT) is based on Fisher's [63] droplet model with a mean-field approximation for the cluster configuration integral. The resulting set of equations can be put in the form of Equation (6) with

$$\Delta F_N = s_1(N_{\text{surf}} - 1)\sigma_{\text{micro}} + (N-1)k_BT\ln(S) \tag{20}$$

and

$$\beta_N = \frac{p_v s_1 N^{2/3}}{(2\pi m_1 k_BT)^{1/2}}, \tag{21}$$

where σ_{micro} is the so-called microscopic surface tension and N_{surf} is the number of molecules at the surface of the cluster. The N molecules composing a cluster are grouped into N_{surf} surface molecules and $(N - N_{\text{surf}})$ core molecules, with $N_{\text{surf}} = N$ if $N \leq N_l$, where N_l is the coordination number of the liquid. The number of molecules at the surface of the cluster and the coordination number of the liquid are estimated by procedures described in Ref. [44] and in the supplemental material of Ref. [64]. The microscopic surface tension is

$$\sigma_{\text{micro}} = -k_BT\ln\left(\frac{-B_2 p_s}{k_BT}\right), \tag{22}$$

where B_2 is the second virial coefficient of the gas. Equations (1), (6), (20), (21), and (22) are mathematically equivalent to the set of equations presented by Kalikmanov [44,62] for the MKNT steady state nucleation rate.

2.4. Semiphenomenological Nucleation Theory

Semiphenomenological nucleation theory (SNT) [65–67] is based on Fisher's [63] droplet model using the virial equation of state, and incorporates several tunable variables.

All of the tunable variables are then usually neglected, except for one or two, and the result [22] can be put in the form of Equation (6) with

$$\Delta F_N = s_1(N^{2/3} - 1)\sigma + (N^{1/3} - 1)\xi - (N - 1)k_B T \ln(S),\tag{23}$$

where the variable ξ has been written [22] in the form

$$\xi = \left(\frac{-1}{2^{1/3} - 1}\right)\left(k_B T \ln\left(\frac{-B_2 p_s}{k_B T}\right) + (2^{2/3} - 1)s_1\sigma\right).\tag{24}$$

The impingement rate is usually estimated by Equation (21).

2.5. Extended Modified Liquid Drop Dynamical Nucleation Theory

The extended modified liquid drop dynamical nucleation theory (EMLDDNT) [61,68,69] considers a small canonical system of M molecules constrained inside a spherical container of volume V at constant temperature. A liquid cluster composed of N molecules formed within the volume is then surrounded by $(M - N)$ ideal gas molecules, and the free energy of the closed system is

$$\Delta F_{c,N} = -Nk_B T \ln\left(\frac{p_v}{p_s}\right) + s_1 N^{2/3}\sigma + N(k_B T - v_1 p_s) + Mk_B T \ln\left(\frac{p_v}{p_0}\right),\tag{25}$$

where $p_v = (M - N)k_B T / (V - v_1 N)$ is the pressure exerted by the $(M - N)$ ideal gas molecules surrounding the cluster and $p_0 = Mk_B T / V$ is the pressure when $N = 0$ and the cluster is not present. In the limit of large M and large V, $p_v \to p_0$ and the CNT expression for the free energy barrier is recovered. The liquid cluster is regarded as a single ideal hard sphere molecule that can collide with other vapor molecules and the rigid wall of the spherical volume, and so the total pressure within the volume is

$$P_N = p_1 + \frac{k_B T}{(4\pi/3)(R - r_N)^3} H(N),\tag{26}$$

where R is the radius of the spherical volume, r_N is the radius of the liquid cluster, and the unit step function $H(N)$ gives the number of liquid clusters present in the volume. The number of molecules composing the liquid cluster is allowed to fluctuate, and the probability of having a cluster of size N is

$$f_N = \frac{\exp\left(-\Delta F_{c,N}/(k_B T)\right)}{\sum_{N=0}^{M} \exp\left(-\Delta F_{c,N}/(k_B T)\right)}.\tag{27}$$

The average pressure within the volume accounting for fluctuations of the cluster size is then

$$P = \sum_{N=0}^{M} f_N P_N,\tag{28}$$

and the total free energy is

$$\Delta F_c = -k_B T \ln\left(\sum_{N=0}^{M} \exp\left(\frac{-\Delta F_{c,N}}{k_B T}\right)\right).\tag{29}$$

The general behavior of the average pressure P is depicted in Figure 1a. When the container volume V is just large enough to contain the M molecules in a large cluster with a few vapor molecules in the small volume remaining, P is very high. As the volume is increased, the pressure initially decreases as some vapor is allowed to evaporate from the cluster until the pressure reaches a local minimum at $V_{\min}$. As the volume increases from $V_{\min}$, the evaporation of the cluster dominates and the pressure increases to a local maximum. As the volume is increased further, the pressure decreases monotonically as the

cluster evaporates completely and the vapor becomes more dilute. The *P*–*V* curve thus has a loop-like shape [61,69]. However, this loop-like shape disappears for *M* less than about 15 due to the effect of fluctuations of the small number of molecules [69].
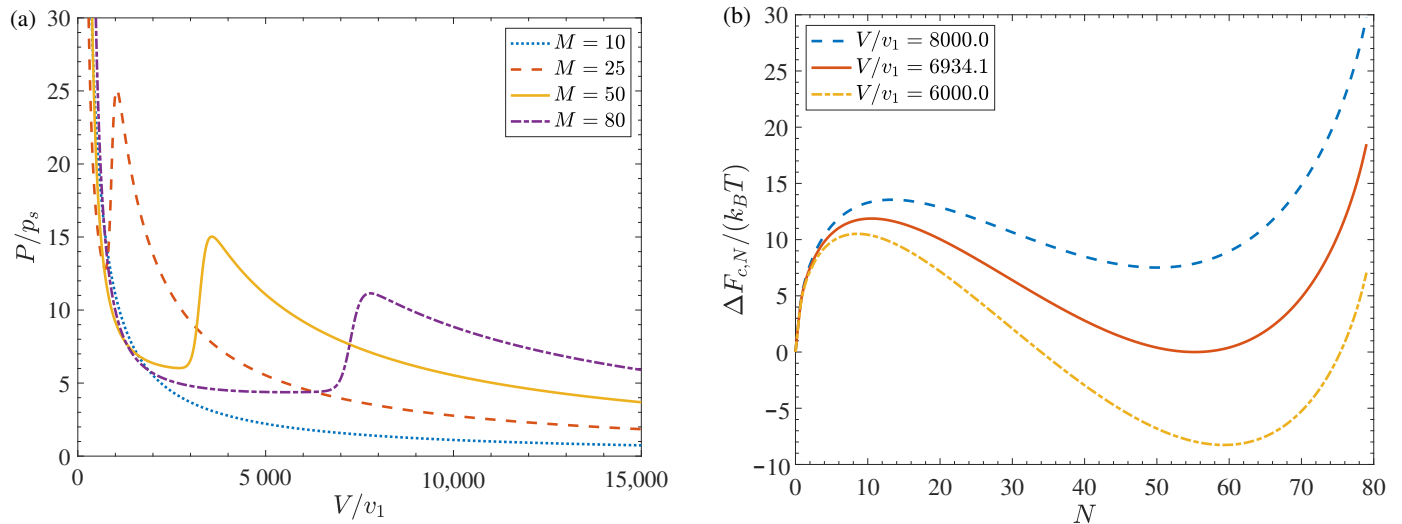
Figure 1. Representative curves for (**a**) *P* and (**b**) $\Delta F_{c,N}$ with $M = 80$, both at $T/T_c = 0.56$.

The general behavior of $\Delta F_{c,N}$ is depicted in Figure 1b. When the volume is chosen to be close to $V_{\min}$, $\Delta F_{c,N}$ starts at zero for $N = 0$ and increases to a local maximum corresponding to the usual critical cluster in unstable equilibrium with the surrounding vapor molecules. As N is increased further, $\Delta F_{c,N}$ decreases to a local minimum corresponding to a stable cluster in constrained equilibrium with the vapor. The cluster cannot continue to grow as it would in an infinite gas because continued growth would result in a depletion of the surrounding vapor, and evaporation from the cluster would cause the cluster to return to its original size. When $V = V_{\min}$, at the local minimum $\Delta F_{c,N} = 0$ and the cluster is said to be metastable. In Figure 1b, $V/v_1 = 6934.1$ corresponds to $V_{\min}$. The metastable cluster is identified as the critical cluster for an infinite gas with saturation ratio $S = p_1/p_s$. Thus, the free energy barrier of the critical cluster in the closed system is characterized by $\Delta F_{c,N} = 0$, $\partial \Delta F_{c,N}/\partial N = 0$, and $\partial^2 \Delta F_{c,N}/\partial N^2 > 0$. The free energy barrier of the critical cluster in the open system of an infinite gas is then

$$\Delta F_N = \Delta F_c - V(p_0 - P) + Mk_BT \ln\left(\frac{p_0}{P}\right), \tag{30}$$

where V and N are chosen to satisfy the above relations and M is adjusted to yield the saturation ratio of the infinite supersaturated gas under consideration. The impingement rate is then obtained from Equation (8) and the nucleation rate from Equation (7).

2.6. Semi-Empirical Density Gradient Theory

Rather than using a capillarity approximation for the liquid cluster, the semi-empirical density gradient theory (SEDGT) of Lax and Leonov [6] regards the cluster as an inhomogeneous fluid with free energy density f, which is a function only of the number density n and the density square gradient $g = (\nabla n)^2$. The free energy density of the fluid is then $f = f_h + \psi$, where f_h is the free energy density of the homogeneous fluid of density n and

$$\psi = \frac{\kappa g}{(1 + \lambda g)^m}, \tag{31}$$

where κ is the influence parameter given below. The constants $\lambda = 9$ and $m = 1/3$ were found [70] by matching the density profiles obtained from molecular dynamic simulations of a Lennard–Jones fluid. The function ψ is often approximated in density gradient theory

by $\psi = \kappa g$. Using the thermodynamic relation $f = n\mu - p$, the free energy barrier of an inhomogeneous droplet is simply

$$\Delta F = \int_V (\Delta f_h + \psi)\mathrm{d}^3\mathbf{r}, \tag{32}$$

where $\Delta f_h = p_v - p_h + n(\mu_h - \mu_v)$. The homogeneous fluid pressure p_h and chemical potential μ_h are obtained from the van der Waals equation of state, $p_h = p_{\mathrm{hs}} - (1/2)\alpha n^2$ and $\mu_h = \mu_{\mathrm{hs}} - \alpha n$. The repulsive terms are provided by the Carnahan–Starling [71] expression for nonattracting hard spheres,

$$p_{\mathrm{hs}} = nk_B T\left(\frac{1 + \eta + \eta^2 - \eta^3}{(1 - \eta)^3}\right), \tag{33}$$

and, using the relation $\partial p_h / \partial n = n(\partial \mu_h / \partial n)$,

$$\mu_{\mathrm{hs}} = k_B T\left(\ln(\eta) + \frac{\eta(8 - 9\eta + 3\eta^2)}{(1 - \eta)^3}\right), \tag{34}$$

where α is the total integrated attractive potential and $\eta = (\pi/6)nd^3$ is the packing fraction of hard spheres of diameter d. The temperature dependent parameters α and d are found from the conditions $p_h(n_l) = p_h(n_v)$ and $\mu_h(n_l) = \mu_h(n_v)$ for the saturated infinite plane fluid.

Since the free energy at equilibrium must satisfy the general condition for a stationary functional $\delta\Delta F(n(\mathbf{r}))/\delta n(\mathbf{r}) = 0$, the density profile of the spherically symmetric critical cluster is determined by

$$2\frac{\mathrm{d}\psi}{\mathrm{d}g}\frac{\mathrm{d}^2 n}{\mathrm{d}r^2} + 4\frac{\mathrm{d}^2\psi}{\mathrm{d}g^2}\left(\frac{\mathrm{d}n}{\mathrm{d}r}\right)^2\frac{\mathrm{d}^2 n}{\mathrm{d}r^2} + \frac{4}{r}\frac{\mathrm{d}\psi}{\mathrm{d}g}\frac{\mathrm{d}n}{\mathrm{d}r} = \mu_h - \mu_v, \tag{35}$$

which is derived in Ref. [6]. Since fluctuations are not considered in SEDGT, the density profile of the critical cluster may be obtained despite the fact that the critical cluster is in an unstable equilibrium rather than a stable one.

The boundary conditions for Equation (35) are $(\mathrm{d}n/\mathrm{d}r)_{r=0} = 0$ and $n(r \to \infty) = n_v$. The density at the center of the finite droplet is not known *a priori* and is usually not equal to the saturated liquid density n_l. The core density of large droplets is greater than n_l due to compressibility effects, since the interior pressure of a droplet is greater than the external gas pressure as given by the Laplace equation, $\Delta p = 2\sigma/r$. However, for small droplets the core density can be significantly lower than the saturated liquid density. Thus, the droplet core density will equal n_l at only one specific droplet size, although it converges to n_l as $S \to 1$ and $N \to \infty$. These trends are depicted in Figure 2, where r_1 is the molecular radius approximated using the volume per molecule in the saturated liquid.

Once the droplet density profile has been found, the free energy barrier of the critical cluster is given by Equation (32) and the number of molecules in the cluster is

$$N = \int_0^\infty (n - n_v)\mathrm{d}^3\mathbf{r}. \tag{36}$$

The surface tension is

$$\sigma = \int_0^\infty (p_N - p_T)\mathrm{d}r, \tag{37}$$

where $p_T = -\Delta f$ is the tangential pressure within the droplet and the normal pressure is given by $(r/2)(\mathrm{d}p_N/\mathrm{d}r) + p_N = p_T$, which has the boundary condition $(\mathrm{d}p_N/\mathrm{d}r)_{r=0} = 0$.
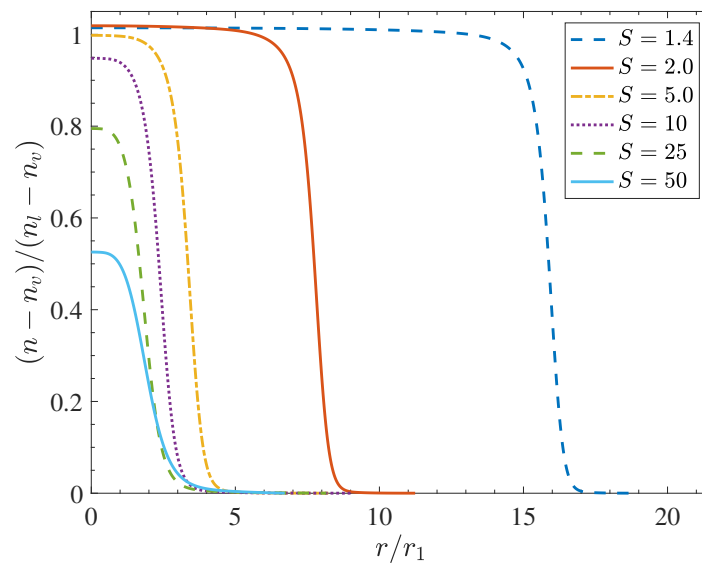
Figure 2. Representative curves for SEDGT droplet density at $T/T_c = 0.56$.

2.7. Scaled Nucleation Rate Model

Hale [21,72,73] has reported a scaled nucleation rate model of the form

$$J = J_0 \exp\left(-\frac{16\pi\Omega^3\left(T_c/T - 1\right)^3}{3\left(\ln(S)\right)^2}\right),$$ (38)

where Ω is the Eötvös constant [74], a measure of the excess surface entropy per molecule. The Eötvös constant is approximately 2 for ordinary liquids. The kinetic prefactor is $J_0 = 1/\lambda_{\text{th}}^3$, where

$$\lambda_{\text{th}} = \frac{h}{(2\pi m_1 k_B T)^{1/2}}$$ (39)

is the thermal de Broglie wavelength and h is the Planck constant. Even though the only fluid properties required by the model are Ω and T_c, the scaled model accurately collapses experimental nucleation rate data for toluene, nonane, and water [21].

2.8. Nonisothermal Nucleation

The above nucleation rate models have implicitly assumed an isothermal process. However, when a condensing molecule binds to the cluster the latent energy of phase change increases the thermal energy of the cluster, warming it. Likewise, the cluster is cooled when a molecule evaporates. Noncondensing impinging molecules can transfer energy to or from the cluster. The isothermal assumption is valid only when there is a large concentration of noncondensing carrier gas molecules, ideally small and light ones [51,75] like helium atoms, that can thermalize the cluster. Feder [76] has performed an irreversible thermodynamics analysis of cluster evolution, and the resulting nonisothermal nucleation rate is

$$J_{\text{noniso}} = \frac{b^2}{b^2 + q^2} J_{\text{iso}}.$$ (40)

The term

$$b^2 = \left(c_v + \frac{1}{2}k_B\right)k_B T^2 + \frac{\beta_{N,c}}{\beta_N}\left(c_{v,c} + \frac{1}{2}k_B\right)k_B T^2$$ (41)

is the mean squared energy fluctuation produced by the impingement of the vapor and carrier gas molecules, where c_v is the specific heat capacity at constant volume per molecule. The term

$$q = h_l - \frac{1}{2}k_B T - \frac{2}{3}\sigma s_1 N^{-1/3}$$ (42)

is the thermal energy released per condensing molecule, where h_l is the latent energy per molecule, $k_B T/2$ is the excess collision energy of the colliding molecule, and $\sigma \partial A/\partial N = (2/3)\sigma s_1 N^{-1/3}$ is the work per molecule required to increase the surface area of the cluster.

2.9. Vibrational Nonequilibrium

Unlike noble gas atoms such as helium or argon, molecules like O_2, N_2, and CO_2 have vibrational energy modes. At low temperatures, molecules are in the ground vibrational energy state, but at higher temperatures, vibrational energy modes can be excited and can begin to affect the clustering process. The transfer of energy from vibrational modes is long compared to the transfer of translational or rotational energy, and at low temperatures, the vibrational relaxation time can be significantly longer than the residence time in the expansion facility. Therefore, in the absence of other processes, after expansion to low temperature the concentration of vibrationally excited molecules initially established in the reservoir is essentially constant and the flow is regarded as "frozen".

When the concentration of vibrationally excited molecules c_{VE} in the condensable vapor is appreciable, the formation process of molecular clusters is fundamentally altered. Vibrationally excited molecules that bind to the cluster will relax to the ground state, reducing the vibrationally excited population and releasing the difference in vibrational energy to the cluster as heat, leading to evaporative cooling. For example, highly vibrationally excited SF_6 has been found [77] to increase the temperature of clusters with $N \approx 40$ by about 45 K, followed by evaporative cooling and complete disintegration of the cluster within about 2 ns.

The relaxation rate of frozen vibrational nonequilibrium flow has been found [78] to be significantly increased in the presence of even small concentrations of a condensable gas. The energy released by the relaxation of a single excited nitrogen molecule in the first vibrational mode is $e = 0.29$ eV [79], which is of similar magnitude to the total binding energy of an $N = 11$ cluster of about $e = 0.27$ eV [80]. It has been observed [81,82] that molecular clusters are not present in hypersonic expansion facilities using air or nitrogen for stagnation temperatures $T_0 > 750 \pm 100$ K, which corresponds to about $c_{VE}/n_v > 0.5$–2%.

For the symmetric stretching mode of CO_2, $c_{VE}/n_v = 0.5$–2% corresponds to a stagnation temperature of about $T_0 = 430 \pm 70$ K, and the energy released by the relaxation of a single vibrationally excited CO_2 molecule is $e = 0.17$ eV. Thus, the clustering process of CO_2 may be appreciably slowed by interaction with vibrationally excited molecules, even at relatively low stagnation temperatures.

3. Results and Discussion

The influence parameter κ is usually determined by matching the calculated infinite plane surface tension to experimental values. In SEDGT, the influence parameter is

$$\kappa = \kappa_\infty + \Delta\kappa, \tag{43}$$

where κ_∞ is found by matching the infinite plane surface tension to experimental values and $\Delta\kappa = \kappa - \kappa_\infty$ is a correction to this value that vanishes at $S = 1$, recovering the infinite plane surface tension. Since a planar liquid interface can not exist at equilibrium for $S > 1$, experimental properties of critical liquid CO_2 clusters, such as σ_*, N_*, or ΔF_*, are required to determine $\Delta\kappa$. In this work, $\Delta\kappa$ is determined by matching experimental nucleation rate values predicted by SEDGT, which are a function of ΔF_*, to the experimental nucleation rates of CO_2 measured by Ref. [10] using a Mach 3.3 supersonic nozzle with expansion from room temperature and a varying concentration of argon carrier gas. The results are

$$\kappa_{\infty*} = 34.93 - 21.06\, T_*^{2.401} \tag{44}$$

and

$$\Delta\kappa_* = -0.32 \frac{\ln(S)}{T_*}, \tag{45}$$

where $T_* = k_B T / \epsilon$ and $\kappa_* = \kappa / (\epsilon \sigma^5)$ are variables nondimensionalized by the Lennard–Jones coefficients given in Appendix A. These equations and the data used to define them are presented in Figure 3. While experimental surface tension values are known with negligible error, the experimental nucleation rate values of Ref. [10] are accurate only to within a factor of 3, which results in the scatter of Figure 3b.
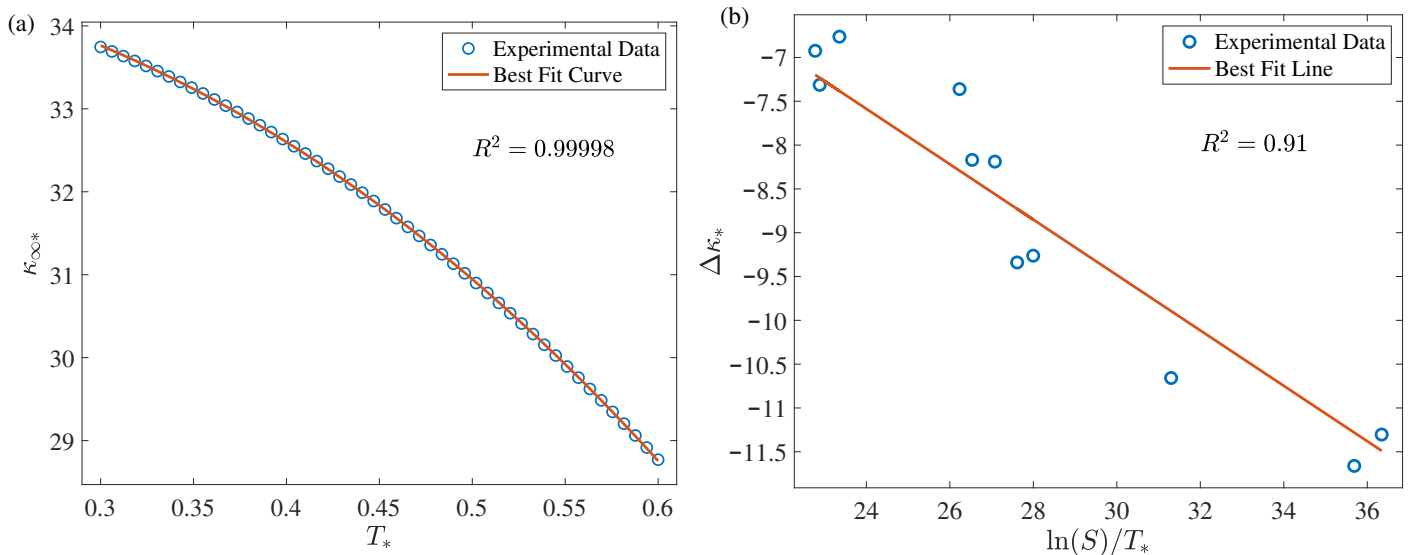
Figure 3. Results for (**a**) $\kappa_{\infty*}$ and (**b**) $\Delta \kappa_*$.

The estimate for the Tolman length obtained from the molecular theory of surface tension (Equation (16)) contains an unknown parameter A. To determine this parameter, the surface tension of critical CO_2 clusters was computed with SEDGT using Equation (37) at the same gas states as those reported in Ref. [10]. The result is

$$A = 3.50 \frac{T}{T_c} - 0.66, \tag{46}$$

which is plotted in Figure 4. The values obtained for A are within the range $\pi/30 \leq A \leq 2.93$ estimated by Ref. [56].

The results of the nucleation rate models discussed in this work are presented in Figure 5 along with the experimental results of Ref. [10]. While experimental uncertainty in nucleation rate studies is usually a factor of 10^{1-2}, the experimental results of Ref. [10] are highly accurate with an estimated experimental uncertainty of a factor of $10^{0.5}$. The log average experimental nucleation rate is $4 \times 10^{23} \, \text{m}^{-3} \text{s}^{-1}$, which is within the typical range for supersonic nozzles [29].

Due to CNT's complete neglect of any small size effects on cluster properties, the nucleation rate estimates of CNT are very poor and are a factor of 10^{5-8} lower than the experiment. As previously documented [21,22], the temperature dependence of the CNT nucleation rate does not agree with the experimental trend and predicts lower nucleation rates at lower temperatures. The estimates of MKNT are similarly poor at a factor of 10^{5-10} lower than experiment. This is likely due to the MKNT estimate for the number of surface molecules of very small clusters. While MKNT implicitly assumes a continuum fluid, it is intended for use as a discrete model with whole numbers of molecules. Therefore, when the number of molecules in the cluster is less than or equal to the coordination number of the fluid, which is $N_l = 8$ for CO_2, MKNT sets the number of surface molecules equal to the number of molecules in the cluster. In CNT and related models, the number of surface molecules is $N^{2/3}$, regardless of the size of the cluster. For a cluster with $N = 8$, MKNT thus estimates twice the number of surface molecules as does CNT. This drastically increases the free energy barrier of the cluster and offsets the reduction in surface energy

achieved by the use of the microscopic surface tension σ_{micro}, which is usually appreciably lower than the infinite plane surface tension σ_∞ used in CNT.
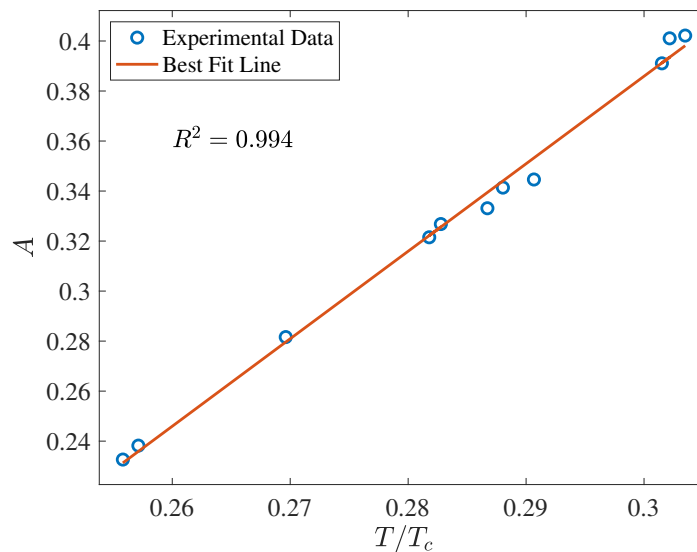
Figure 4. Results for A.

When small size effects on the surface tension are considered through the use of Tolman's equation (Equation (15)), the results of CNT are greatly improved. The Tolman length estimated from the molecular theory of surface tension [56] given by Equation (16) actually results in a nucleation rate a factor of 10^2 greater than the experimental rate, and can be considered a "conservative" estimate for the nucleation rate. Notably, the temperature dependence matches the experimental trend. However, the Tolman length estimated from molecular dynamics simulations [57] given by Equation (17) is less successful, underestimating experimental rates by a factor of 10^{2-6} with the same temperature dependence as uncorrected CNT. The CNT expression with the Courtney [60] $1/S$ correction term is referred to here as equilibrium CNT (ECNT), since the $1/S$ correction results from using the equilibrium cluster concentration obtained from the equilibrium saturated gas rather than the actual metastable gas. The temperature dependence of ECNT with the Tolman length estimate of Equation (16) are similar to those of CNT with Equation (16), but the nucleation rate is underestimated by a factor of 10^2. The experimental nucleation rate is thus bracketed by the nucleation rates of CNT with Equation (16) and ECNT with Equation (16).

The results of the scaled model (Equation (38)) are poor at a factor of 10^{3-5} lower than the experiment, but the temperature dependence is improved over CNT. While the SNT nucleation rate is close to the experimental value at low temperature, since the temperature dependence is similar to that of CNT, the nucleation rate is greatly overestimated at higher temperatures and is overall is a factor of 10^{1-4} greater than the experiment.

The nucleation rates estimated by SCCNT, EMLDDNT, and SEDGT are all very close to the experimental nucleation rate over the entire temperature range, although SCCNT and EMLDDNT deviate by a factor of up to $10^{1-1.5}$ at high temperature. The results of SEDGT match both the magnitude and the temperature dependence of the experimental nucleation rates, which is due to the fact that the empirical correction to the influence parameter $\Delta\kappa$ is tuned to the experimental nucleation rates. This correction factor is designed to be extrapolated, and it has previously been shown [6] that the nucleation rates obtained by SEDGT agree with experimental nitrogen nucleation rates across a wide range of temperatures, pressures, and nucleation rates. The success of EMLDDNT is likely due to the explicit consideration of microscale fluctuations in the formation of the critical cluster, even though the model uses the same capillarity approximation as CNT.

SCCNT and EMLDDNT yield extremely similar nucleation rates across the entire experimental temperature range. This is remarkable considering the dissimilarity of the

models. However, due to the fault in the theory of SCCNT discussed in Section 2.2, the success of SCCNT here must be viewed as a coincidence arising from the large scaling factor (Equation (19)) present in the SCCNT nucleation rate expression rather than an example of the greater theoretical validity of the model.
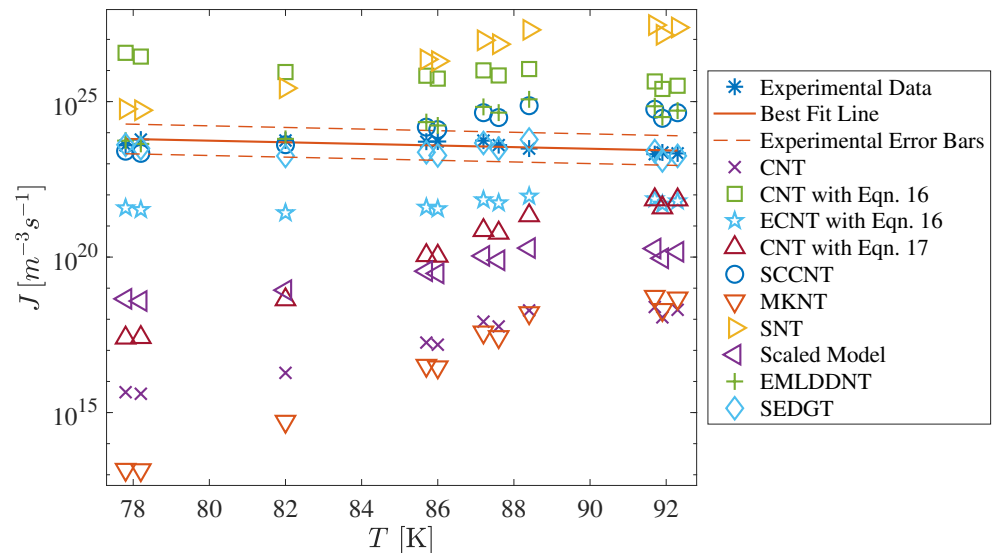
Figure 5. Model results for nucleation rate compared to experiment [10].

4. Experimental and Simulation Results

CO$_2$ condensation onset was measured at the University of Notre Dame's SBR-50 [83,84]. The SBR-50 is a supersonic blowdown wind tunnel with Mach 2 and Mach 4 nozzles and Ohmic heaters in the high pressure tank. The stagnation temperature range is $T_0 = 300$–750 K, the stagnation pressure range is $p_0 = 1$–4.5 bar, and the run time is up to 1 second. To prevent adiabatic cooling of the high pressure gas during a run, the facility recompresses the expanding high pressure gas to keep the gas temperature constant. The cross section at the end of the nozzle is 76.2×76.2 mm, and the upper and lower test section walls have a 1 degree half-angle expansion to compensate for boundary layer growth.

In the present study, a $1.2 \pm 0.05\%$ mole fraction CO$_2$ mixture was obtained by adding CO$_2$ (Airgas CD LZP200) to air that was filtered and dried to a dew point of 212 K at 0.7 MPa or about 2.5 ppm using a desiccant air drier (Sullair DMD-80) and passing the mixture through a static in-line mixer before adding it to the high pressure tank. The stagnation pressure p_0 was set, and the stagnation temperature T_0 was adjusted until condensation onset was detected in the test section using the Mach 4 nozzle. The estimated uncertainty in T_0 is 4 K, and the estimated uncertainty in p_0 is 0.05 bar. Condensation onset was detected using laser Rayleigh scattering gas density measurements performed using a frequency doubled ns pulsed Nd:YAG laser (Quanta-Ray DCR-4) and a CCD camera (pco.2000). The laser was focused into the test section through a fused silica window using a 2 m focal length fused silica plano-convex lens. Since the Rayleigh scattering intensity is $I \sim d^6$, where d is the diameter of the scattering object, condensation onset is easily detected by the sudden and anomalous increase in measured freestream density.

The above experiment was simulated using the three most accurate nucleation rate model evaluated: SCCNT, EMLDDNT, and SEDGT. Hill's [6,85] one-dimensional forms of the conservation of mass, momentum, and energy for a condensable ideal gas are used, which are stepped downstream using an explicit Euler method. The displacement thickness of the turbulent boundary layer is estimated using the method of Sivells [86]. The droplet growth rate after nucleation is estimated using the model of Gyarmathy [87], which is valid for the entire Knudsen number range while also accounting for the droplet surface temperature, droplet interior mean temperature, and droplet slip velocity. Since the critical cluster is in equilibrium with the surrounding gas, to prevent numerical difficulties,

the suggestion of Hill [85] is followed and the droplet is not introduced to the growth rate model until $r \geq 1.3r_*$. Condensation onset is defined by $g/g_{max} = 0.01$, where g is the condensate mass fraction, $g_{max} = cR_{mix}/R_{CO2}$ is the condensate mass fraction after complete condensation, and c is the CO_2 mole fraction.

The current experimental and simulated condensation onset results are presented in Figure 6 along with other experimental data [10,15,25,88–91]. An overview of these expansion facilities is presented in Table 1. There are more condensation onset points from the work of Dingilian et al. [10] than there are nucleation rate values in Figure 5 because, while 24 condensation onset points are reported by Ref. [10], only 11 nucleation rate values are reported. The experimental condensation onset points of Tanimura et al. [88] are for heterogeneous nucleation of CO_2 onto H_2O ice particles, and so are near the liquid vapor pressure line. This is additional confirmation that the phase of critical clusters is liquid-like rather than solid-like. The work of Duff [15] is at high pressure, and the nucleation rate is not measured. The results of Ref. [15] are divided into two groups corresponding to the two different nozzles used, and thus the two different nucleation rates obtained by the study. The work of Ramos et al. [89], Lippe et al. [90], and Krohn et al. [91] use small supersonic free jets, obtaining very high saturation ratios. While experimental nucleation rates are reported by Ref. [91], the gas state is identified as being near or past the spinodal, so the phase transition is second order rather than first order and a critical cluster does not exist. Tadayon [25] reports condensation from a supersonic jet with a fixed orifice. While Ref. [25] provides estimated nucleation rates, they are not very accurate.
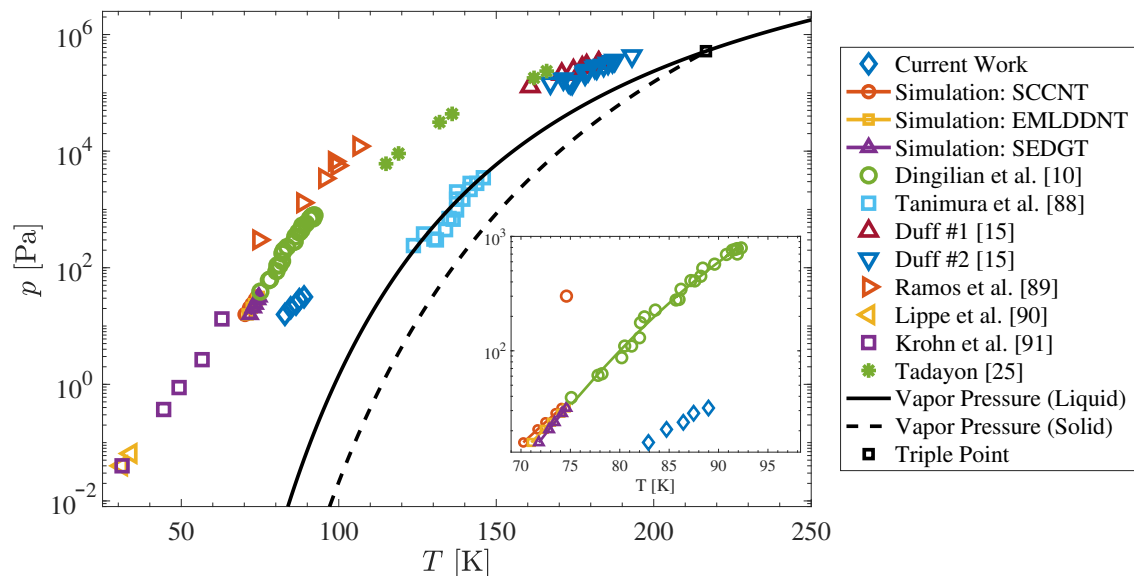
Figure 6. Experimental and simulation results for CO_2 condensation onset point.

The simulation results for all three nucleation rate models agree with each other and with study of Dingilian et al. [10], although the three models have slightly different temperature variation. However, the current experimental results for condensation onset are between the saturated liquid vapor pressure line and the simulation results. It is hypothesized that the difference between experimental and simulation results is due to heterogeneous nucleation resulting from the presence of a trace amount of a condensable vapor, such as a hydrocarbon. A hydrocarbon vapor could originate from the fast valve of the facility, which uses a hydrocarbon-based lubricant, and condense in the nozzle, forming condensation nuclei. However, efforts to remove lubricant exposed to the gas flow resulted in only a minor increase in saturation ratio at condensation onset.

The slope of the condensation onset points is different than other studies, with the lower pressure onset points at much lower temperatures. This may also be indicative

of heterogeneous nucleation, since at lower pressures and higher saturation ratios, the heterogeneous nucleation rate decreases relative to the homogeneous nucleation rate [92].

Table 1. Overview of expansion facilities.

Facility Type	Carrier	CO_2 [%]	T [K]	p_v [Pa]	S	Ref.
de Laval Nozzle	Air	1.2	88–97	16–32	606–2.9×10^3	Present
Planar Nozzle	Ar	2.0–39.3	75–92	39–793	2.3×10^3–6.1×10^4	[10]
Planar & de Laval	–	100	161–193	1.3×10^5–4.3×10^5	2.7–7.8	[15]
Fixed Orifice Free Jet	He	5–100	115–166	6.1×10^3–2.4×10^5	9.3–146	[25]
de Laval Nozzle	N_2	2.4–25.2	124–146	240–3.5×10^3	0.5–1.4	[88]
Fixed Orifice Free Jet	–	100	75–106	301–1.2×10^4	1.8×10^3–2.2×10^6	[89]
de Laval Nozzle	$Ar + CH_4$	7	31–34	0.04–0.065	1.1×10^{23}–3.3×10^{26}	[90]
de Laval Nozzle	$Ar + CH_4$	0.12–50	31–63	0.04–13	1.1×10^8–1.8×10^{26}	[91]

The residence time of the expansion facility, defined here as the time spent by a freestream molecule between the saturated gas state and the condensation onset point, or $\Delta t_R = t_{\text{onset}} - t_{S=1}$, is longer in the SBR-50 facility than in the facility of Dingilian et al. [10], due partly to the larger size of the SBR-50 facility. The average residence time in the SBR-50 facility is about $\Delta t_R = 460\,\mu s$, while the average residence time of the facility of Dingilian et al. [10] is about $\Delta t_R = 80\,\mu s$. Since the residence time in the SBR-50 facility is about 6 times longer than that of Dingilian et al. [10], more time is available for nucleation to occur and the condensation onset points in the SBR-50 facility should occur slightly closer to the saturated liquid vapor pressure line than those of Dingilian et al. [10]. This effect can be seen be seen in the work of Duff [15], which uses two different nozzles. Even though the overall size of the nozzles are similar, the expansion rate and thus the residence times of the nozzles are different, resulting in one set of condensation onset points occurring slightly closer to the saturated liquid vapor pressure line than the other.

The SBR-50 simulation results are consistent with the experimental onset points of Dingilian et al. [10], and the effects of a longer residence time are not seen. This discrepancy could be due to the difference in expansion rates at condensation onset of the two facilities. The expansion rate is characterized here by the parameter $\tau_e = (\mathrm{d}\ln(S)/\mathrm{d}t)^{-1}$, which has units of time and can be considered a characteristic expansion time. Since the SBR-50 facility uses a de Laval nozzle [93], rapid initial expansion is followed by cancellation of characteristic lines at the end of the nozzle. The expansion rate at condensation onset is low and is set by the 1 degree half angle expansion of the top and bottom test section walls. The characteristic expansion time at condensation onset is about $\tau_e = 260\,\mu s$. Dingilian et al. [10] uses a simple nozzle with planar walls and continuous expansion of the gas, and the average characteristic expansion time at condensation onset is about $\tau_e = 8\,\mu s$. Since this is on the same order as the transient nucleation rate characteristic time τ_t, the transient nucleation rate may not be adequately approximated by the steady state nucleation rate in the expansion facility of Dingilian et al. [10]. Since the transient nucleation rate is always lower than the steady state nucleation rate, the nucleation rates obtained by Dingilian et al. [10] may be slightly lower than steady state nucleation rates at equivalent gas states. Since the steady state nucleation rate models considered here are evaluated by comparison to the experimental nucleation rates of Dingilian et al. [10], they may slightly underestimate the actual steady state nucleation rate, and when used in flowfield simulations may slightly overestimate the saturation ratio at condensation onset.

The condensation onset points of the current work correspond to stagnation temperatures of $T_0 = 350$–375 K. As noted in Section 2.9, affects of the interaction of vibrationally excited CO_2 with nucleating clusters are expected to become discernible at stagnation temperatures near $T_0 = 430 \pm 70$ K, resulting in a delay or complete suppression of nu-

cleation. These affects are not seen here. It is possible that the vibrationally excited CO_2 population is reduced or eliminated by interaction with the nucleating hydrocarbon vapor discussed above.

The affects of the transient nucleation rate and vibrational nonequilibrium require further investigation.

5. Conclusions

Several classical and non-classical nucleation rate models have been presented and compared to each other and experimental values for the homogeneous nucleation rate of CO_2 in supersonic nozzles. The most accurate of these models are self-consistent classical nucleation theory (SCCNT), extended modified liquid drop dynamical nucleation theory (EMLDDNT), and semi-empirical density gradient theory (SEDGT), although a flaw has been pointed out in the theory of SCCNT.

Experimental results for the condensation onset point of CO_2 in a supersonic nozzle have been presented and compared to other experiments and flowfield simulations of the condensing gas. It is found that all three models are consistent with each other and with the experimental results of Ref. [10]. However, the current experimental results acquired at the SBR-50 facility using a Rayleigh scattering technique appear to be affected by heterogeneous nucleation due to the presence of a trace amount of a condensable vapor, and the current experimental results do not agree with simulation results of homogeneous nucleation. Several hypotheses have been discussed and require further investigation.

All models considered here are reduced order and assume, either implicitly or explicitly, that the density of the critical cluster of molecules is continuous. Highly accurate results and deeper physical insight will require the explicit consideration of the cluster as a group of discrete molecules interacting with each other and the surrounding vapor molecules and undergoing constant microscale fluctuations.

Nomenclature

A	Temperature dependent variable in Equation (16)
b	Mean squared energy fluctuation of impinging molecules
B_2	Second virial coefficient of the vapor
c	Concentration (mole fraction)
c_v	Specific heat at constant volume per molecule of the vapor
$c_{v,c}$	Specific heat at constant volume per molecule of the carrier gas
d	Hard sphere diameter
e	Energy
f_h	Homogeneous free energy density
f_N	Probability of cluster existing in EMLDDNT volume
g	Density square gradient, $(\nabla n)^2$, *or* condensate mass fraction
g_{max}	Condensate mass fraction with complete condensation
h	Planck constant
h_l	Latent energy of phase change per molecule

H	Unit step function
J	Steady state nucleation rate
J_{iso}	Isothermal steady state nucleation rate
J_{noniso}	Nonisothermal steady state nucleation rate
J_t	Transient nucleation rate
k_B	Boltzmann constant
m_1	Mass per molecule
M	Number of molecules
n	Number density of molecules
n_v	Number density of free molecules in the vapor
n_l	Saturated liquid number density
n_N	Number density of clusters with N molecules
$n_{N,e}$	Equilibrium number density of clusters
n_s	Saturated vapor number density
N	Number of molecules in the cluster
N_l	Coordination number of the liquid
N_*	Number of molecules in critical cluster
p_0	Stagnation pressure *or* EMLDDNT pressure without cluster
p_1	Vapor pressure within EMLDDNT volume
p_c	Pressure of carrier gas
p_h	Pressure of homogeneous fluid
p_{hs}	Hard sphere pressure
p_N	SEDGT normal pressure
p_s	Saturated vapor pressure
p_v	Pressure of vapor
p_T	SEDGT tangential pressure
P	Average pressure in EMLDDNT volume
P_N	Total pressure within EMLDDNT volume
q	Thermal energy released per condensing molecule
r	Radius of droplet *or* radius within droplet
r_1	Radius of molecule
R	Radius of EMLDDNT volume *or* ideal gas constant
s_1	Saturated liquid surface area per molecule
S	Saturation ratio, p_v/p_s
T	Temperature
T_c	Critical point temperature
T_*	Nondimensional temperature, $k_B T/\epsilon$
v_1	Saturated liquid volume per molecule
V	Volume
Z	Zel'dovich factor
α	Total integrated attractive potential
α_N	Cluster evaporation rate
β_N	Cluster impingement rate
β_*	Impingement rate onto critical cluster
δ_T	Tolman length
ΔF_c	Total free energy within EMLDDNT closed volume
$\Delta F_{c,N}$	Closed system free energy barrier of droplet with N molcules
ΔF_N	Free energy barrier of cluster with N molecules
ΔF_*	Free energy barrier of critical cluster
Δp	Pressure difference between cluster and gas
Δt_R	Residence time of freestream molecule
$\Delta \kappa$	SEDGT influence parameter correction factor, $\kappa - \kappa_\infty$
$\Delta \kappa_*$	Nondimensional SEDGT influence parameter correction factor, $\kappa_* - \kappa_{\infty *}$
$\Delta \mu$	Difference in chemical potential
$\Delta \mu_h$	Difference in chemical potential of homogeneous fluid
$\Delta \mu_{\text{hs}}$	Hard sphere difference in chemical potential
ϵ	Lennard–Jones potential

η	Packing fraction of hard spheres
κ_l	Isothermal compressibility of the liquid
κ	SEDGT influence parameter
κ_∞	SEDGT infinite plane influence parameter
$\kappa_{\infty *}$	Nondimensional SEDGT infinite plane influence parameter
κ_*	Nondimensional SEDGT influence parameter, $\kappa/(\epsilon\sigma^5)$
λ_{th}	Thermal de Broglie wavelength
ζ	SNT variable (Equation (24))
σ	Surface tension *or* Lennard-Jones zero energy distance
σ_∞	Infinite plane surface tension
τ_e	Characteristic time for gas expansion
τ_t	Characteristic time for transient nucleation
ψ	Inhomogeneous free energy density
Ω	Eötvös constant

Appendix A. Fluid Properties

The molecular mass of CO_2 is 44.009 g/mol. The Lennard–Jones parameters are $\sigma = 0.3753$ nm and $\epsilon/k_B = 246.1$ K [94]. The critical temperature is $T_c = 304.1282$ K, the critical pressure is $p_c = 7.3773$ MPa, and the critical density is $\rho_c = 467.6$ kg/m^3 [95]. The characteristic vibrational temperature of the CO_2 symmetric stretching mode is $\theta_v = 1946$ K [96], and the characteristic vibrational temperature of nitrogen is $\theta_v = 3398$ K [97]. The saturated liquid vapor pressure of CO_2 [95] is

$$\ln\left(\frac{p_s}{p_c}\right) = \frac{T_c}{T}\sum_{i=1}^{4} a_i\left(1 - \frac{T}{T_c}\right)^{t_i}, \tag{A1}$$

where $a_1 = -7.0602087$, $a_2 = 1.9391218$, $a_3 = -1.6463597$, $a_4 = -3.2995634$, $t_1 = 1$, $t_2 = 1.5$, $t_3 = 2$, and $t_4 = 4$. The infinite plane surface tension of the saturated liquid [98] is

$$\sigma_\infty[\text{N/m}] = 5.902 \times 10^{-5}(304.26 - T)^{1.25}. \tag{A2}$$

The saturated liquid density [95] is

$$\ln\left(\frac{\rho_s}{\rho_c}\right) = \sum_{i=1}^{4} a_i\left(1 - \frac{T}{T_c}\right)^{t_i}, \tag{A3}$$

where $a_1 = 1.9245108$, $a_2 = -0.62385555$, $a_3 = -0.32731127$, $a_4 = 0.39245142$, $t_1 = 0.34$, $t_2 = 0.5$, $t_3 = 10/6$, and $t_4 = 11/6$. The second virial coefficient of the vapor is estimated [99] by

$$\frac{B_2 p_c}{k_B T_c} = f_0 + \omega f_1, \tag{A4}$$

where the functions are $f_0 = 0.1445 - 0.330(T/T_c)^{-1} - 0.1385(T/T_c)^{-2} - 0.0121(T/T_c)^{-3} - 0.000607(T/T_c)^{-8}$ and $f_1 = 0.0637 + 0.331(T/T_c)^{-2} - 0.423(T/T_c)^{-3} - 0.008(T/T_c)^{-8}$, and the acentric factor is $\omega = 0.225$. The specific heat at constant volume of the saturated liquid is approximated for $T < 233$ K by

$$c_v[\text{J kg}^{-1}\,\text{K}^{-1}] = \exp\left(b_1(T - b_2)\right) + b_3, \tag{A5}$$

where $b_1 = 0.0884485$, $b_2 = 191.95686$, and $b_3 = 1944.03256$ were obtained using data from Ref. [100]. The enthalpy of vaporization is approximated by a single value, $\Delta H_{\text{vap}} = 3.73 \times 10^5$ J/kg [101]. The thermal conductivity of the saturated liquid is approximated for $T < T_c$ by $k[\text{W m}^{-1}\,\text{K}^{-1}] = k_0 + \Delta k$ [102], where

$$k_0 = \frac{1}{1000}\left(\frac{T}{T_c}\right)^{1/2}\left[\sum_{i=0}^{3}\frac{L_k}{(T/T_c)^k}\right]^{-1}, \tag{A6}$$

with $L_0 = 0.0151874307$, $L_1 = 0.0280674040$, $L_2 = 0.0228564190$, and $L_3 = -0.00741624210$, and

$$\Delta k = \frac{1}{1000} \sum_{i=1}^{6} \left[B_{1,i} + B_{2,i} \left(\frac{T}{T_c} \right) \right] \left(\frac{\rho_s}{\rho_c} \right)^i, \tag{A7}$$

with $B_{1,1} = 0.0100128$, $B_{1,2} = 0.0560488$, $B_{1,3} = -0.0811620$, $B_{1,4} = 0.0624337$, $B_{1,5} = -0.0206336$, $B_{1,6} = 0.00253248$, $B_{2,1} = 0.00430829$, $B_{2,2} = -0.0358563$, $B_{2,3} = 0.0671480$, $B_{2,4} = -0.0522855$, $B_{2,5} = 0.0174571$, and $B_{2,6} = -0.00196414$.

References

1. Lakebrink, M.T.; Bowcutt, K.G.; Winfree, T.; Huffman, C.C.; Juliano, T.J. Optimization of a Mach-6 Quiet Wind-Tunnel Nozzle. *J. Spacecr. Rocket.* **2018**, *55*, 315–321. [CrossRef]
2. Daum, F.L.; Gyarmathy, G. Condensation of Air and Nitrogen in Hypersonic Wind Tunnels. *Am. Inst. Aeronaut. Astronaut.* **1967**, *6*, 458–465. [CrossRef]
3. Faro, I.; Small, T.R.; Hill, F.K. The Supersaturation of Nitrogen in a Hypersonic Wind Tunnel. *J. Appl. Phys.* **1952**, *23*, 40–43. [CrossRef]
4. Willmarth, W.W.; Nagamatsu, H.T. The Condensation of Nitrogen in a Hypersonic Nozzle. *J. Appl. Phys.* **1952**, *23*, 1089–1095. [CrossRef]
5. Tans, P.; Keeling, R. Trends in Atmospheric Carbon Dioxide; NOAA Global Monitoring Laboratory. Available online: https://gml.noaa.gov/ccgg/trends/data.html (accessed on 1 November 2021).
6. Lax, P.A.; Leonov, S.B. Semiempirical Model for Homogeneous Nitrogen Condensation in Hypersonic Wind Tunnels. *AIAA J.* **2020**, *58*, 4807–4818. [CrossRef]
7. Goglia, G.L. Limit of Supersaturation of Nitrogen Vapor Expanding in a Nozzle. Ph.D. Thesis, University of Michigan, Ann Arbor, MI, USA, 1959.
8. Zahoransky, R.A. Nitrogen Nucleation in an Unsteady Supersonic Flow Field. *Z. Für Flugwiss. Und Weltraumforsch.* **1986**, *10*, 34–37.
9. Steinwandel, J. Homogeneous Condensation of Nitrogen in the Expansion Wave of a Cryogenic Shock Tube. *Berichte Bunsenges. Phys. Chem.* **1985**, *89*, 481–484. [CrossRef]
10. Dingilian, K.K.; Halonen, R.; Tikkanen, V.; Reischl, B.; Vehkamäki, H.; Wyslouzil, B.E. Homogeneous nucleation of carbon dioxide in supersonic nozzles I: Experiments and classical theories. *Phys. Chem. Chem. Phys.* **2020**, *22*, 19282–19298. [CrossRef] [PubMed]
11. Wood, S.E. Nucleation and Growth of CO_2 Ice Crystals in the Martian Atmosphere. Ph.D. Thesis, University of California Los Angeles, Los Angeles, CA, USA, 1999.
12. Brown, K.W. Coherent Raman Spectroscopy of Non-Polar Molecules and Molecular Clusters. Ph.D. Thesis, Oregon State University, Corvallis, OR, USA, 1991.
13. Mayer, S.G. Size Estimates of Molecular Clusters Using Elastic Light Scattering and CARS Spectroscopy. Ph.D. Thesis, Oregon State University, Corvallis, OR, USA, 1997.
14. Erbland, P.J.; Rizzetta, D.P.; Miles, R.B. Numerical and Experimental Investigation of CO_2 Condensate Behavior in Hypersonic Flow. In Proceedings of the 21st AIAA Aerodynamic Measurement Technology and Ground Testing Conference, Denver, CO, USA, 19–22 June 2000; Paper No. 2000-2379, [CrossRef]
15. Duff, K.M. Non-Equilibrium Condensation of Carbon Dioxide in Supersonic Nozzles. Ph.D. Thesis, Massachusetts Institute of Technology, Cambridge, MA, USA, 1966.
16. Ozawa, T.; Suzuki, T.; Fujita, K. Investigation of Condensation Effect in CO_2 Hypersonic Rarefied Flows. In Proceedings of the 54th AIAA Aerospace Sciences Meeting, San Diego, CA, USA, 4–8 January 2000; Paper No. 2016-1729, [CrossRef]
17. Kumar, R.; Li, Z.; Levin, D.A. Modeling of carbon dioxide condensation in the high pressure flows using the statistical BGK approach. *Phys. Fluids* **2011**, *23*, 052001. [CrossRef]
18. Horsch, M.; Lin, Z.; Windmann, T.; Hasse, H.; Vrabec, J. The air pressure effect on the homogeneous nucleation of carbon dioxide by molecular simulation. *Atmos. Res.* **2011**, *101*, 519–526. [CrossRef]
19. Horsch, M.; Vrabec, J.; Bernreuther, M.; Grottel, S.; Reina, G.; Wix, A.; Schaber, K.; Hasse, H. Homogeneous nucleation in supersaturated vapors of methane, ethane, and carbon dioxide predicted by brute force molecular dynamics. *J. Chem. Phys.* **2008**, *128*, 164510. [CrossRef]
20. Li, Z.; Zhong, J.; Levin, D.A. Modeling of CO_2 Homogeneous and Heterogeneous Condensation Plumes. *J. Phys. Chem. C* **2010**, *114*, 5276–5286. [CrossRef]
21. Hale, B.N. Temperature dependence of homogeneous nucleation rates for water: Near equivalence of the empirical fit of Wölk and Strey, and the scaled nucleation model. *J. Chem. Phys.* **2005**, *122*, 204509. [CrossRef] [PubMed]
22. Tanaka, K.K.; Kawamura, K.; Tanaka, H.; Nakazawa, K. Tests of the homogeneous nucleation theory with molecular-dynamics simulations. I. Lennard-Jones molecules. *J. Chem. Phys.* **2005**, *122*, 184514. [CrossRef] [PubMed]
23. Merikanto, J.; Zapadinsky, E.; Lauri, A.; Vehkamäki, H. Origin of the Failure of Classical Nucleation Theory: Incorrect Description of the Smallest Clusters. *Phys. Rev. Lett.* **2007**, *98*, 145702. [CrossRef] [PubMed]

24.　Holten, V.; Labetski, D.G.; van Dongen, M.E.H. Homogeneous nucleation of water between 200 and 240 K: New wave tube data and estimation of the Tolman length. *J. Chem. Phys.* **2005**, *123*, 104505. [CrossRef]

25.　Tadayon, P. Determination of Interfacial Tension from Optical Measurements of Nucleation Rates. Ph.D. Thesis, Oregon State University, Corvallis, OR, USA, 1998.

26.　Desgranges, C.; Delhommelle, J. Free energy calculations along entropic pathways. I. Homogeneous vapor-liquid nucleation for atomic and molecular systems. *J. Chem. Phys.* **2016**, *145*, 204112. [CrossRef]

27.　Kido, A.; Nakanishi, K. Molecular dynamics study of nucleation in supersaturated vapor of carbon dioxide. *Fluid Phase Equilibria* **1999**, *158–160*, 79–86. [CrossRef]

28.　Halonen, R.; Tikkanen, V.; Reischl, B.; Dingilian, K.K.; Wyslouzil, B.E.; Vehkamäki, H. Homogeneous nucleation of carbon dioxide in supersonic nozzles II: Molecular dynamics simulations and properties of nucleating clusters. *Phys. Chem. Chem. Phys.* **2021**, *23*, 4517–4529. [CrossRef]

29.　Iland, K. Experimente zur homogenen Keimbildung von Argon und Stickstoff. Ph.D. Thesis, Universität zu Köln, Köln, Germany, 2004.

30.　Jortner, J. Cluster size effects. *Z. Phys. Atoms Mol. Clust.* **1992**, *24*, 247–275. [CrossRef]

31.　Hoare, M.; Pal, P. Physical cluster mechanics: Statistical thermodynamics and nucleation theory for monatomic systems. *Adv. Phys.* **1975**, *24*, 645–678. [CrossRef]

32.　Hoare, M.; Pal, P. Physical cluster mechanics: Statics and energy surfaces for monatomic systems. *Adv. Phys.* **1971**, *20*, 161–196. [CrossRef]

33.　Torchet, G.; de Feraudy, M.; Boutin, A.; Fuchs, A.H. Structural transformation in $(CO_2)_N$ clusters, N<100. *J. Chem. Phys.* **1996**, *105*, 3671–3678. [CrossRef]

34.　Maillet, J.B.; Boutin, A.; Fuchs, A.H. From molecular clusters to bulk matter. II. Crossover from icosahedral to crystalline structures in CO_2 clusters. *J. Chem. Phys.* **1999**, *111*, 2095–2102. [CrossRef]

35.　Castleman, A.W.; Keesee, R.G. Clusters: Properties and Formation. *Annu. Rev. Phys. Chem.* **1986**, *37*, 525–550. [CrossRef]

36.　Maillet, J.B.; Boutin, A.; Fuchs, A.H. The Melting Phase Transition in Small Carbon Dioxide Clusters. *Mol. Simul.* **1997**, *19*, 285–299. [CrossRef]

37.　Rytkönen, A.; Valkealahti, S.; Manninen, M. Melting and evaporation of argon clusters. *J. Chem. Phys.* **1997**, *106*, 1888–1892. [CrossRef]

38.　Doye, J.P.K.; Calvo, F. Entropic effects on the structure of Lennard-Jones clusters. *J. Chem. Phys.* **2002**, *116*, 8307–8317. [CrossRef]

39.　Maillet, J.B.; Boutin, A.; Buttefey, S.; Calvo, F.; Fuchs, A.H. From molecular clusters to bulk matter. I. Structure and thermodynamics of small CO_2, N_2, and SF_6 clusters. *J. Chem. Phys.* **1998**, *109*, 329–337. [CrossRef]

40.　Acevedo, A.J.; Caballero, L.M.; López, G.E. Phase transitions in molecular clusters. *J. Chem. Phys.* **1997**, *106*, 7257–7261. [CrossRef]

41.　Ford, I.J. Nucleation theorems, the statistical mechanics of molecular clusters, and a revision of classical nucleation theory. *Phys. Rev. E* **1997**, *56*, 5615–5629. [CrossRef]

42.　Ellerby, H.M. Distribution of density fluctuations in a molecular theory of vapor-phase nucleation. *Phys. Rev. E* **1994**, *49*, 4287–4297. [CrossRef]

43.　Vehkamäki, H. *Classical Nucleation Theory in Multicomponent Systems*; Springer: Berlin/Heidelberg, Germany, 2006. [CrossRef]

44.　Kalikmanov, V.I. *Nucleation Theory*; Lecture Notes in Physics; Springer: Berlin/Heidelberg, Germany, 2013; Volume 860. [CrossRef]

45.　Abraham, F.F. *Homogeneous Nucleation Theory: The Pretransition Theory of Vapor Condensation*; Academic Press: Cambridge, MA, USA, 1974; [CrossRef]

46.　Friedlander, S.K. *The Mechanics of Aerosols*, 2nd ed.; Oxford University Press: Oxford, UK, 2000.

47.　Zel'dovich, J.B. K Teorii Obrazovaniya Novoy Fazy. Kavitatsiya. *Zhurnal Eksperimental'noy Teor. Fiziki* **1942**, *12*, 525–538.

48.　Lothe, J.; Pound, G.M. Statistical Mechanics of Nucleation. In *Nucleation*; Zettlemoyer, A.C., Ed.; Marcel Dekker: New York, NY, USA, 1969; Chapter 3, pp. 109–149.

49.　Wakeshima, H. Time Lag in the Self-Nucleation. *J. Chem. Phys.* **1954**, *22*, 1614–1615. [CrossRef]

50.　Wu, D.T. The time lag in nucleation theory. *J. Chem. Phys.* **1992**, *97*, 2644–2650. [CrossRef]

51.　Wedekind, J.; Hyvärinen, A.P.; Brus, D.; Reguera, D. Unraveling the "Pressure Effect" in Nucleation. *Phys. Rev. Lett.* **2008**, *101*, 125703. [CrossRef]

52.　Tolman, R.C. The Effect of Droplet Size on Surface Tension. *J. Chem. Phys.* **1949**, *17*, 333–337. [CrossRef]

53.　Rowlinson, J.S.; Widom, B. *Molecular Theory of Capillarity*, 1st ed.; International Series of Monographs on Chemistry; Oxford University Press: New York, NY, USA, 1982; Volume 8.

54.　Gránásy, L. Semiempirical van der Waals/Cahn-Hilliard theory: Size dependence of the Tolman length. *J. Chem. Phys.* **1998**, *109*, 9660–9663. [CrossRef]

55.　Koga, K.; Zeng, X.C. Validity of Tolman's equation: How large should a droplet be? *J. Chem. Phys.* **1998**, *109*, 4063–4070. [CrossRef]

56.　Wang, X.S.; Zhu, R.Z. Relation between Tolman length and isothermal compressibility for simple liquids. *Chin. Phys. B* **2013**, *22*, 036801. [CrossRef]

57.　Horsch, M.; Vrabec, J.; Hasse, H. Modification of the classical nucleation theory based on molecular simulation data for surface tension, critical nucleus size, and nucleation rate. *Phys. Rev. E* **2008**, *78*, 011603. [CrossRef] [PubMed]

58. Girshick, S.L.; Chiu, C.P. Kinetic nucleation theory: A new expression for the rate of homogeneous nucleation from an ideal supersaturated vapor. *J. Chem. Phys.* **1990**, *93*, 1273–1277. [CrossRef]
59. Wilemski, G. The Kelvin equation and self-consistent nucleation theory. *J. Chem. Phys.* **1995**, *103*, 1119–1126. [CrossRef]
60. Courtney, W.G. Remarks on Homogeneous Nucleation. *J. Chem. Phys.* **1942**, *35*, 2249–2250. [CrossRef]
61. Reguera, D.; Bowles, R.K.; Djikaev, Y.; Reiss, H. Phase transitions in systems small enough to be clusters. *J. Chem. Phys.* **2003**, *118*, 164720. [CrossRef]
62. Kalikmanov, V.I. Mean-field kinetic nucleation theory. *J. Chem. Phys.* **2006**, *124*, 124505. [CrossRef] [PubMed]
63. Fisher, M.E. The theory of condensation and the critical point. *Physics* **1967**, *3*, 255–283. [CrossRef]
64. Sinha, S.; Bhabhe, A.; Laksmono, H.; Wölk, J.; Strey, R.; Wyslouzil, B. Argon nucleation in a cryogenic supersonic nozzle. *J. Chem. Phys.* **2010**, *132*, 064304. [CrossRef]
65. Laaksonen, A.; Ford, I.J.; Kulmala, M. Revised parametrization of the Dillmann-Meier theory of homogeneous nucleation. *Phys. Rev. E* **1994**, *49*, 5517–5524. [CrossRef]
66. Delale, C.F.; Meier, G.E.A. A semiphenomenological droplet model of homogeneous nucleation from the vapor phase. *J. Chem. Phys.* **1993**, *98*, 9850–9858. [CrossRef]
67. Dillmann, A.; Meier, G.E.A. A refined droplet approach to the problem of homogeneous nucleation from the vapor phase. *J. Chem. Phys.* **1991**, *94*, 3872–3884. [CrossRef]
68. Reguera, D.; Reiss, H. Fusion of the Extended Modified Liquid Drop Model for Nucleation and Dynamical Nucleation Theory. *Phys. Rev. Lett.* **2004**, *93*, 165701. [CrossRef]
69. Reguera, D.; Reiss, H. Extended Modified Liquid Drop-Dynamical Nucleation Theory (EMLD-DNT) Approach to Nucleation: A New Theory. *J. Phys. Chem. B* **2004**, *108*, 19831–19842. [CrossRef]
70. Baidakov, V.G.; Boltachev, G.S. Extended version of the van der Waals capillarity theory. *J. Chem. Phys.* **2004**, *121*, 8594–8601. [CrossRef]
71. Carnahan, N.F.; Starling, K.E. Equation of State for Nonattracting Rigid Spheres. *J. Chem. Phys.* **1969**, *51*, 635–636. [CrossRef]
72. Hale, B.N. Application of a scaled homogeneous nucleation-rate formalism to experimental data at $T \ll T_c$. *Phys. Rev. A* **1986**, *33*, 4156–4163. [CrossRef] [PubMed]
73. Hale, B.N. The Scaling of Nucleation Rates. *Metall. Trans. A* **1992**, *23*, 1863–1868. [CrossRef]
74. Palit, S.R. Thermodynamic Interpretation of the Eötvös Constant. *Nature* **1956**, *177*, 1180. [CrossRef]
75. Wedekind, J.; Reguera, D.; Strey, R. Influence of thermostats and carrier gas on simulations of nucleation. *J. Chem. Phys.* **2007**, *127*, 064501. [CrossRef] [PubMed]
76. Feder, J.; Russel, K.C.; Lothe, J.; Pound, G.M. Homogeneous nucleation and growth of droplets in vapours. *Adv. Phys.* **1966**, *15*, 111–178. [CrossRef]
77. Makarov, G.; Petin, A. Disintegration of Ar_N, Kr_N, and $(N_2)_N$ Clusters during Collisions with Highly Vibrationally Excited SF_6 Molecules. *J. Exp. Theor. Phys.* **2014**, *146*, 398–405. [CrossRef]
78. Sharma, S.P.; Ruffin, S.M.; Gillespie, W.D.; Meyer, S.A. Vibrational relaxation measurements in an expanding flow using spontaneous Raman scattering. *J. Thermophys. Heat Transf.* **1993**, *7*, 697–703. [CrossRef]
79. Vincenti, W.G.; Kruger, C.H. *Introduction to Physical Gas Dynamics*; John Wiley and Sons: New York, NY, USA, 1967.
80. Kobraei, H.R.; Anderson, B.R. Formation energies and concentrations of microclusters for homogeneous nucleation. *J. Chem. Phys.* **1988**, *88*, 4451–4459. [CrossRef]
81. Balla, R.J.; Everhart, J.L. Rayleigh Scattering Density Measurements, Cluster Theory, and Nucleation Calculations at Mach 10. *Am. Inst. Aeronaut. Astronaut.* **2012**, *50*, 698–707. [CrossRef]
82. Balla, R.J.; Rhode, M.N.; Everhart, J.L. Supersaturation Total Temperature, Pitot Pressure, and Rayleigh Scattering Measurements at Mach 10. *Am. Inst. Aeronaut. Astronaut.* **2014**, *52*, 1452–1465. [CrossRef]
83. Elliott, S.; Hasegawa, M.; Sakaue, H.; Leonov, S. Shock-dominated flow control by plasma array: Pressure analysis including pressure-sensitive paint visualization. *Exp. Therm. Fluid Sci.* **2022**, *131*, 110522. [CrossRef]
84. Houpt, A.; Hedlund, B.; Leonov, S.; Ombrello, T.; Carter, C. Quasi-DC electrical discharge characterization in a supersonic flow. *Exp. Fluids* **2017**, *58*, 1–17. [CrossRef]
85. Hill, P.G. Condensation of Water Vapour during Supersonic Expansion in Nozzles. *J. Fluid Mech.* **1966**, *25*, 593–620. [CrossRef]
86. Sivells, J.C. Aerodynamic design of axisymmetric hypersonic wind-tunnel nozzles. *J. Spacecr. Rocket.* **1970**, *7*, 1292–1299. [CrossRef]
87. Gyarmathy, G. The Spherical Droplet in Gaseous Carrier Streams: Review and Synthesis. In *Multiphase Science and Technology*; Hewitt, G.F., Delhaye, J.M., Zuber, N., Eds.; McGraw-Hill: New York, NY, USA, 1982; Volume 1, Chapter 2, pp. 99–279.
88. Tanimura, S.; Park, Y.; Amaya, A.; Modak, V.; Wyslouzil, B.E. Following heterogeneous nucleation of CO_2 on H_2O ice nanoparticles with microsecond resolution. *RSC Adv.* **2015**, *5*, 105537–105550. [CrossRef]
89. Ramos, A.; Fernández, J.M.; Tejeda, G.; Montero, S. Quantitative study of cluster growth in free-jet expansions of CO_2 by Rayleigh and Raman scattering. *Phys. Rev. A* **2005**, *72*, 053204. [CrossRef]
90. Lippe, M.; Szczepaniak, U.; Hou, G.L.; Chakrabarty, S.; Ferreiro, J.J.; Chasovskikh, E.; Signorell, R. Infrared Spectroscopy and Mass Spectrometry of CO_2 Clusters during Nucleation and Growth. *J. Phys. Chem. A* **2019**, *123*, 2426–2437. [CrossRef] [PubMed]
91. Krohn, J.; Lippe, M.; Li, C.; Signorell, R. Carbon dioxide and propane nucleation: The emergence of a nucleation barrier. *Phys. Chem. Chem. Phys.* **2020**, *22*, 15986–15998. [CrossRef] [PubMed]

92. Liu, X.Y. Heterogeneous nucleation or homogeneous nucleation? *J. Chem. Phys.* **2000**, *112*, 9949–9955. [CrossRef]
93. Anderson, J.D. *Modern Compressible Flow: With Historical Perspective*, 3rd ed.; McGraw-Hill: New York, NY, USA, 2003.
94. Clifford, A.A.; Gray, P.; Platts, N. Lennard-Jones 12:6 parameters for ten small molecules. *J. Chem. Soc. Faraday Trans.* **1977**, *73*, 381–382. [CrossRef]
95. Span, R.; Wagner, W. A New Equation of State for Carbon Dioxide Covering the Fluid Region from the Triple- Point Temperature to 1100 K at Pressures up to 800 MPa. *J. Phys. Chem. Ref. Data* **1996**, *25*, 1509–1596. [CrossRef]
96. Herzberg, G. *Molecular Spectra and Molecular Structure II. Infrared and Raman Spectra of Polyatomic Molecules*; D. Van Nostrand Company: New York, NY, USA, 1945.
97. Irikura, K.K. Experimental Vibrational Zero-Point Energies: Diatomic Molecules. *J. Phys. Chem. Ref. Data* **2007**, *36*, 389–397. [CrossRef]
98. Jasper, J.J. The Surface Tension of Pure Liquid Compounds. *J. Phys. Chem. Ref. Data* **1972**, *1*, 841–1010. [CrossRef]
99. Poling, B.E. *Properties of Gases and Liquids*, 5th ed.; McGraw-Hill Education: New York, NY, USA, 2001.
100. Magee, J.W. Specific heats (C_v) of saturated and compressed liquid and vapor carbon dioxide. *Int. J. Thermophys.* **1986**, *7*, 1163–1182. [CrossRef]
101. Acree, W.; Chickos, J.S. Phase Transition Enthalpy Measurements of Organic and Organometallic Compounds. Sublimation, Vaporization and Fusion Enthalpies from 1880 to 2015. Part 1. C_1-C_{10}. *J. Phys. Chem. Ref. Data* **2016**, *45*, 033101. [CrossRef]
102. Huber, M.L.; Sykioti, E.A.; Assael, M.J.; Perkins, R.A. Reference Correlation of the Thermal Conductivity of Carbon Dioxide from the Triple Point to 1100 K and up to 200 MPa. *J. Phys. Chem. Ref. Data* **2016**, *45*, 013102. [CrossRef] [PubMed]